Anisotropic properties, charge ordering, and ferrimagnetic structures in the strongly correlated β-V_2PO_5 single crystal

Jie Xing,[1] Huibo Cao,[2] Arpita Paul,[3] Chaowei Hu,[4] Hsin-Hua Wang,[4] Yongkang Luo,[4] Raj Chaklashiya,[4] Jared M. Allred,[5] Stuart Brown,[4] Turan Birol,[3] and Ni Ni[1,*]

[1]*Department of Physics and Astronomy and California NanoSystems Institute, University of California, Los Angeles, California 90095, USA*
[2]*Neutron Scattering Division, Oak Ridge National Laboratory, Oak Ridge, Tennessee 37831, USA*
[3]*Department of Chemical Engineering and Materials Science, University of Minnesota, Minnesota 55455, USA*
[4]*Department of Physics and Astronomy, University of California, Los Angeles, California 90095, USA*
[5]*Department of Chemistry and Biochemistry, University of Alabama, Tuscaloosa, Alabama 35487, USA*

(Received 27 December 2017; accepted 11 September 2020; published 28 September 2020)

Single crystal β-V_2PO_5 was synthesized by chemical vapor transport method and characterized by transport, thermodynamic, neutron diffraction, nuclear magnetic resonance measurements and first-principles calculation. It was shown to be a semiconductor with a band gap of 0.48 eV, undergoing a charge ordering (unusual V^{2+} and V^{3+}) phase transition accompanied by a tetragonal to monoclinic structural distortion at 610 K and a paramagnetic to ferrimagnetic phase transition at 128 K with a propagation vector of $\mathbf{k} = 0$. The easy axis is in the monoclinic *ac* plane pointing 47(9)° away from the monoclinic *a* axis. This collinear ferrimagnetic structure and anisotropic isothermal magnetization measurements suggest weak magnetic anisotropy in this compound. The first-principles calculations indicate that the intrachain interactions in the face-sharing VO_6 chains dominate the magnetic hamiltonian and identify the Γ_5^+ normal mode of the lattice vibration to be responsible for the charge ordering and thus the structural phase transition.

DOI: 10.1103/PhysRevMaterials.4.094414

I. INTRODUCTION

Charge ordering(CO), the long-range ordering of transition metal ions with different oxidization states, is a prominent feature in mixed valent 3*d* transition metal oxides [1]. Due to the strong Coulomb interaction in the charge ordering state, a high-symmetry to low-symmetry structural distortion can occur, accompanied with the sudden enhancement in the electrical resistivity arising from the charge localization. The competition between this charge disproportionation and the exchange interactions among magnetic transition metal ions has led to emergent phenomena, such as colossal magnetoresistance in $RE_{1-x}A_xMnO_3$ (RE = rare earth, A = alkaline earth) [2,3], superconductivity in β-$Ag_{0.33}V_2O_5$ [4].

The vanadium phosphorus oxide system (V-P-O) has distinct structural stacking and variable valences of vanadium, providing a great avenue to investigate the structure-property relationship, enriching our understanding on the competition of CO and various exchange interaction. The fundamental building blocks of the V-P-O system consist of VO_6 octahedra or VO_4 tetrahedra linked by PO_4 tetrahedra with valence P^{5+}. Rich 3*d* vanadium magnetism and valences have been observed. For example, VPO_4 with V^{3+} ions, containing one dimensional chains of edge-sharing VO_6 octahedra, undergoes an incommensurate antiferromagnetic (AFM) phase transition at 26 K and then a commensurate AFM phase transition at 10.3 K [5]. α-$VO(PO_3)_2$ with one dimensional chains of corner-sharing VO_6 octahedra, is AFM at 1.9 K with valence V^{4+} [6]. Mixed valence V^{3+} and V^{4+} antiferromagnetically couple together below 5 K in $V_2(VO)(P_2O_7)_2$, where segments of edge-sharing VO_4 tetrahedra and VO_6 octahedra exist [7]. Alternating V^{4+} spin-chain model can be used to describe the magnetism in $(VO)_2P_2O_7$ with corner and edge-sharing VO_6 octahedra ladders [8–12]. Also, MM'$(VO)(PO_4)_2$ compounds with frustrated square-lattice vanadium layers are model compounds for applying the J_1-J_2 Heisenberg model in low dimension (2D) [13–15].

Recently, β-V_2PO_5, containing chains of face-sharing VO_6 octahedra linked by PO_4 tetrahedra in the tetragonal phase [16], was proposed as a ferromagnetic (FM) topological Weyl and node-line semimetal without any trivial band at the Fermi level [17].

In this paper, we performed a combined study of the single crystalline β-V_2PO_5 by x-ray and neutron diffraction as well as NMR, transport and thermodynamic measurements, to investigate the nature of these two transitions. Anisotropic magnetization was found between $H//ab$ and $H \perp ab$. As a powerful characterized method of magnetism, single crystal neutron diffraction was performed from 4 to 650 K. Similar to the previously reported charge ordering in β-Fe_2PO_5 [18], β-V_2PO_5 presents a charge ordering transition accompanied by a tetragonal to monoclinic structural distortion at 610 K and a paramagnetic to ferrimagnetic phase transition at 128 K with a propagation vector of $\mathbf{k} = 0$. Our results based on single crystal study is consistent with the recent powder work on the β-V_2PO_5 [19,20]. The magnetic structure indicates that the easy axis is in the monoclinic *ac* plane pointing 47(9)°

*Corresponding author: nini@physics.ucla.edu

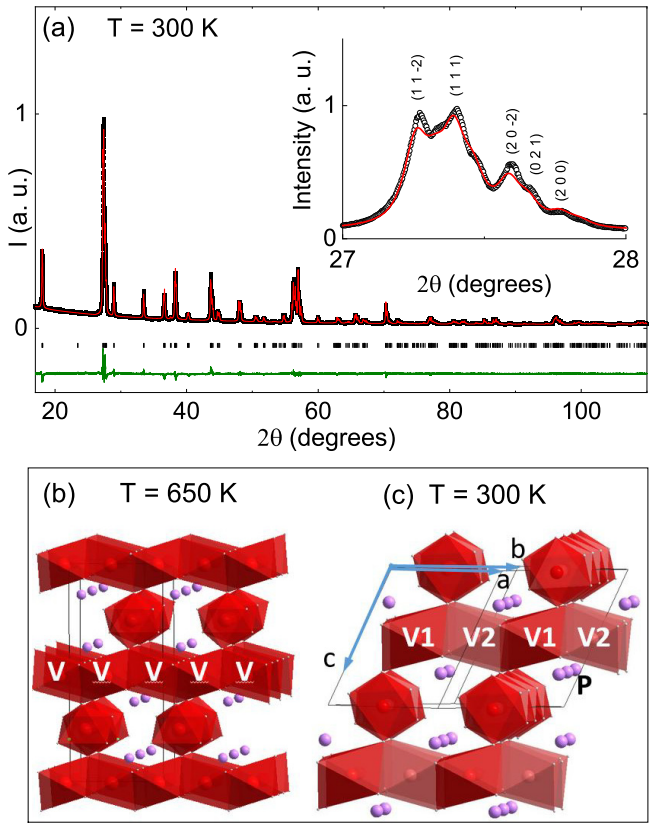

FIG. 1. (a) The experimental and refined powder x-ray diffraction patterns for β-V_2PO_5 at 300 K. Black: experimental pattern. Red: refined pattern. Green: the difference between the experimental and refined patterns. Black ticks: the Bragg peak positions in the monoclinic structure. (Inset) Enlarged view from 27° to 28°. [(b) and (c)] The crystal structure of β-V_2PO_5 at (b) 650 and (c) 300 K.

away from the monoclinic a axis. Based on the experimental results, the first-principles calculations indicate that the intra-chain interactions in the face-sharing VO_6 chains dominate the magnetic Hamiltonian and identify the Γ_5^+ normal mode of the lattice vibration to be responsible for the charge ordering and thus the structural phase transition.

II. EXPERIMENTAL METHODS

Precursor β-V_2PO_5 powder was made by solid state reaction. V_2O_5 powder and phosphorus chunks were weighed according to the stoichiometric ratio 1 : 1 and sealed in a quartz tube under vacuum. The ampule was slowly heated up to 600 °C and dwelled for 2 hours, and then was increased to 1000 °C and stayed for 2 days before it was quenched in water. The resultant β-V_2PO_5 (~2 g) powder and iodine flakes (10 mg/cm^3) were loaded into a 15-cm long quartz tube and sealed under vacuum. Single crystals of β-V_2PO_5 were then grown by chemical vapor transport method [16]. The hot end was set at 1000°C and the cold end was set at 900°C. After two weeks, quite a few sizable three dimensional single crystals (~4 mm × 4 mm × 2mm) were found at the cold end. The detailed crystal structures of β-V_2PO_5 are presented in Fig. 1.

Throughout the paper, *ab* plane is the plane where chains locate in. The $(hkl)_T$ means the peak indexed in the tetragonal structure while $(hkl)_M$ means the peak indexed in the monoclinic structure.

Magnetic properties were measured in a Quantum Design (QD) Magnetic Properties Measurement System (MPMS3). A single crystal around 20 mg with a polished *ab* surface and a single crystal with as-grown (011) surface were used. Temperature dependent heat capacity was measured in a QD Dynocool Physical Properties Measurement System (Dynocool PPMS) using the relaxation technique at zero field. To enhance the thermal contact and lower the measurement time, the β-V_2PO_5 single crystal was ground into powder and then mixed with silver powder according to the mass ratio of 1 : 1. The heat capacity of β-V_2PO_5 was then obtained by subtracting the heat capacity of silver [21]. Below 200 K, the two wire ETO(Electrical Transport Option) method was used for the electric resistivity measurement in PPMS. From 200 to 400 K, the electric resistivity was measured with standard four-point method while above 400 K, it was measured in a homemade high temperature resistivity probe. The small kink in the resistivity around 350 K is due to the temperature control of the instrument.

Single crystal neutron diffraction was performed at the HB-3A four-circle diffractometer equipped with a 2D detector at the High Flux Isotope Reactor (HFIR) at ORNL. Neutron wavelength of 1.546 Å was used from a bent perfect Si-220 monochromator [22]. The pyrolytic graphite (PG) filter was used before the sample to reduce the half-λ neutrons. Representational analysis with *SARAh* [23] was run to search for the possible magnetic symmetries. The nuclear and magnetic structure refinements were carried out with the FULLPROF SUITE [24]. Powder x-ray diffraction measurements were performed using a PANalytical Empyrean diffractometer (Cu K_α radiation).

Nuclear magnetic resonance (NMR) measurement was done under a fixed magnetic field of approximately 8.5 T, applied along the direction perpendicular to the *ab* plane, where the chains locate in. The spectra were collected by performing an optimized $\pi/2$-τ-π spin-echo pulse sequence. The spin-lattice relaxation time T_1 was measured by integration of the phase corrected real part of the spin echo using the saturation-recovery technique [25] and spin echo decay time T_2 was measured by altering τ in the sequence. Spin-lattice relaxation time T_1 is obtained by the magnetization recovery fitting to a single exponential form.

First-principles density functional theory calculations were performed to compare the energies of different magnetic configurations. We used Projector augmented-wave method (PAW) as implemented in Vienna *ab initio* simulation package (VASP) with PBEsol exchange correlation functional [26–28]. A 8 × 8 × 8 k-point grid and the energy cutoff of 500 eV ensures convergence in the primitive cell with four formula units.

III. EXPERIMENTAL RESULTS

Figure 1(a) present the refinement of the powder x-ray diffraction taken at room temperature by monoclinic structure of β-V_2PO_5. The neutron data at 4.5 and 300 K can be well

TABLE I. The crystal structure of the β-V_2PO_5 phase at 4.5, 300, and 650 K, respectively.

β-V_2PO_5 at 4.5 K monoclinic $C2/c$			
$a = 7.563$ Å	$b = 7.563$ Å	$c = 7.235$ Å	$\beta = 121.51^\circ$
$R_{F^2} = 0.0691$	$wR_{F^2} = 0.0841$	$R_F = 0.044$	$\chi^2 = 19.2$
site	x/a	y/b	z/c
V1	0	1/2	0
V2	1/4	1/4	0
O1	0.066(3)	0.749(2)	0.632(2)
O2	0.317(2)	0.496(2)	0.598(1)
O3	0	0.652(2)	1/4
P	0	0.121(2)	1/4
β-V_2PO_5 at 300 K monoclinic $C2/c$			
$a = 7.570$ Å	$b = 7.570$ Å	$c = 7.232$ Å	$\beta = 121.56^\circ$
$R_{F^2} = 0.0734$	$wR_{F^2} = 0.0956$	$R_F = 0.0473$	$\chi^2 = 25.1$
site	x/a	y/b	z/c
V1	0	1/2	0
V2	1/4	1/4	0
O1	0.065(3)	0.749(2)	0.630(2)
O2	0.318(2)	0.496(2)	0.599(1)
O3	0	0.652(2)	1/4
P	0	0.119(3)	1/4
β-V_2PO_5 at 650K Tetragonal $I41/amd$			
$a = 5.357(2)$ Å	$b = 5.357(2)$ Å	$c = 12.373(4)$Å	
$R_{F^2} = 0.0707$	$wR_{F^2} = 0.0888$	$R_F = 0.0421$	$\chi^2 = 5.12$
site	x/a	y/b	z/c
V1	1/4	1/4	1/4
P1	0	3/4	1/8
O1	0	−0.012(1)	0.193(4)
O2	0	3/4	5/8

fitted with this $C2/c$ monoclinic symmetry, whereas the result at 650 K can be fitted by the tetragonal structure. This finding suggests a tetragonal to monoclinic phase transition between 300 and 650 K, consistent with the study on the powder sample [19,20]. The detailed crystal structures at 4.5, 300, and 650 K determined from neutron data are summarized in Table I. The high-temperature tetragonal and low-temperature monoclinic structures are visualized in Figs. 1(b) and 1(c), respectively.

In the monoclinic phase, the monoclinic c axis is 121.45° from the ab plane which is the plane where the chains sit in. The unique V site in the tetragonal structure separates into V1 and V2 sites with the V1 atoms and V2 atoms alternately locating along each chain direction [V1 and V2 sites are labeled in Fig. 1(c)], as a result, the average bond length of VO_6 octahedra on V1 site increases while that on V2 site decreases. Bond-valence analysis of the monoclinic crystal structure assigns charges of 2.0(1) and 2.9(1) to V_1 and V_2 respectively, which is a proof of very different bonding environments of the two V ions [29,30]. This strongly suggests charge ordering in the β-V_2PO_5 single crystal.

Figures 2(a)–2(c) show the anisotropic magnetic properties of β-V_2PO_5 single crystal at $H//ab$ and $H \perp ab$. The inset of Fig. 2(a) shows a β-V_2PO_5 single crystal against 1 mm scale. Figure 2(a) presents the temperature dependent M/H taken at $H = 1$ kOe from 2 to 250 K in zero-field-cooled (ZFC) and field-cooled(FC) mode with H parallel and perpendicular to the ab plane. The sharp upturns of the curves and the bifurcation was observed in ZFC and FC data for both directions below $T_{\text{mag}} \sim 128$ K. The smooth ZFC and FC curves suggest no other magnetic transition below T_{mag}. Comparing with the other V-O-P materials, the magnetic transition temperature is quite high [5–7], suggesting strong exchange interactions. Figure 2(b) shows the temperature dependent M/H (blue) and H/M (black) measured from 300 to 1000 K with $H // (011)_T$ at $H = 10$ kOe. We see a subtle but discernible enhancement in M/H at the characteristic temperature $T_{co} = 610$ K. Linear Curie-Weiss behavior can be seen from 1000 to 800 K in H/M. By fitting M/H from 1000 to 800 K using the Curie-Weiss formula $M/H = C/(T - \theta_{\text{cw}})$, where C is the Curie constant and θ_{cw} is the Weiss temperature, we obtained effective magnetic moment $\mu_{\text{eff}} = 3.63\ \mu_B$/V and $\theta_{\text{cw}} = -730$ K (μ is the Bohr magneton). The μ_{eff} is larger than the one of $V^{2.5+}$ (the effective moment of an equal mixture of V^{2+} and V^{3+}) but comparable to the one of V^{2+}. The large negative θ_{cw} suggests antiferromagnetic interaction between vanadium ions.

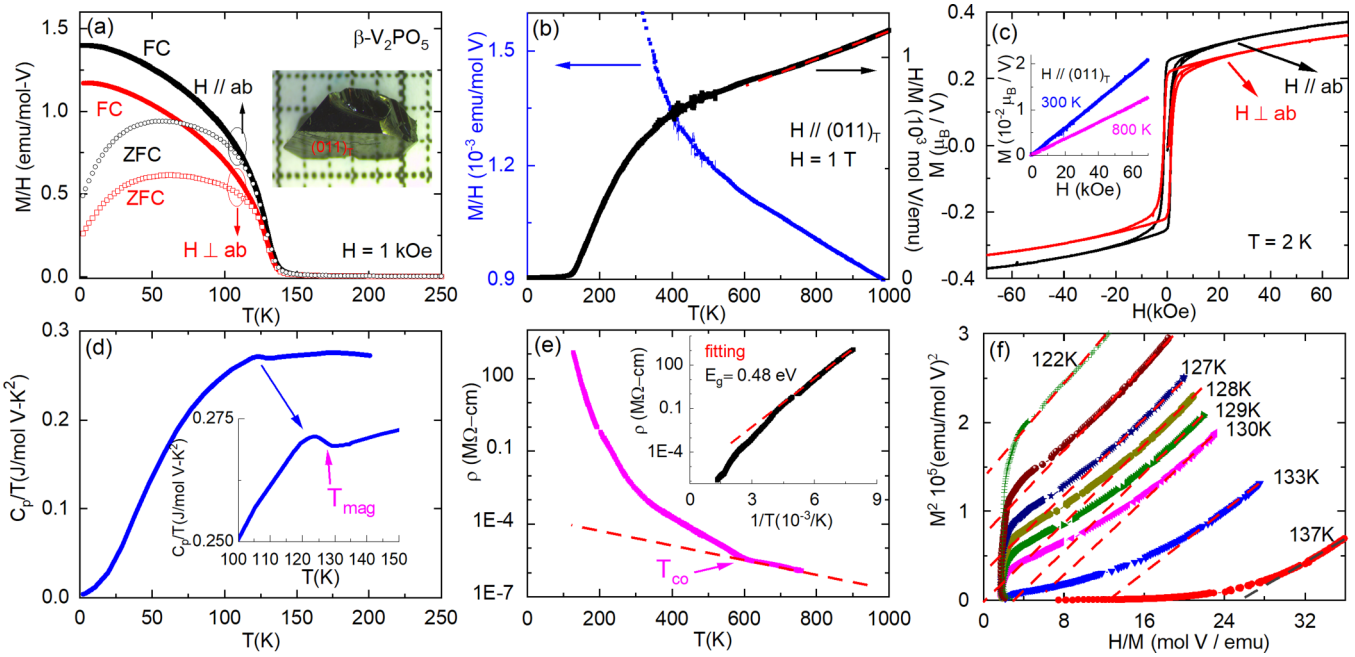

FIG. 2. (a) ZFC and FC M/H vs T under $H = 1$ kOe with $H//ab$ and $H \perp ab$ from 2 to 250 K. (Inset) Picture of β-V_2PO_5 single crystal against 1-mm scale. (b) H/M and M/H vs T under $H = 10$ kOe with $H//(011)_T$ from 2 to 1000 K. The red lines are the fitting curves. (c) Isothermal $M(H)$ curves at 2 K with $H//ab$ and $H \perp ab$. Inset: $M(H)$ curves at 300 and 800 K along $H//(011)_T$. (d) Specific heat C_p vs T from 2 to 200 K. (Inset) C_p/T vs T near $T_{\rm mag}$. (e) Resistivity ρ vs T from 130 to 760 K. The red line emphasizes the transition at $T_{\rm CO}$. (Inset) ρ vs $1/T$. Red line: the fitting curve using the thermal excitation model. (f) The Arrott plot at various temperatures from 122 to 137 K.

Figure 2(c) shows the anisotropic field dependent magnetization $M(H)$ taken at 2 K with $H//ab$ and $H \perp ab$. The crystal orientation was determined by x-ray diffraction. Clear hysteresis can be observed in both directions. Both curves show similar shape and magnitude, suggesting weak magnetic anisotropy in this system. The coercive fields are around 1.3 kOe for both. The estimated saturation moment is extracted by the linear fitting from 60 to 70 kOe along two directions at 2 K. The remnant moments are 0.22 μ_B/V for $H \perp ab$ and 0.25 μ_B/V for $H//ab$ and the saturation moments are 0.26 μ_B/V for $H \perp ab$ and 0.30 μ_B/V for $H//ab$, which are so much smaller than the saturation moment of V^{2+} $(d^3)(3.87\mu_B)$ and V^{3+} $(d^2)(2.83\mu_B)$ ions in the octahedral coordination, agreeing with ferrimagnetism below $T_{\rm mag}$. The inset of Fig. 2(c) shows the $M(H)$ curves taken at 300 and 800 K with $H // (011)_T$. Both curves are linear with the applied magnetic field without hysteresis. Figure 2(d) shows the temperature dependent C_p/T data (blue) taken from 2 K to 200 K. The inset shows the relation between C_p/T and T near $T_{\rm mag}$. A heat capacity anomaly featuring a second-order magnetic transition appears around 128 K, accompanying with the magnetic phase transition observed in Fig. 2(a).

Figure 2(e) shows the resistivity (ρ) of the β-V_2PO_5 single crystals versus temperature from 130 K up to 760 K. Similar to the powder sample [19], a semiconductor behavior was found in the single crystal instead of the semi-metal suggested by the theoretical prediction [17]. A semiconductor to semiconductor phase transition is discernible at 610 K, which confirms the phase transition at T_{co} suggested by the subtle susceptibility increase shown in Fig. 2(b). ρ versus reciprocal temperature is plotted in the inset of Fig. 2(d). By fitting the data between 280 to 130 K with the thermal excitation model $\rho(T) = \rho(0)\exp(E_g/2k_BT)$, the estimated gap size of β-V_2PO_5 is 0.48 eV. The gap value is similar to 0.45–0.57 eV of the vanadium phosphate glass [31]. Arrott plot (M^2 versus H/M) has been widely used to determine the phase transition temperature [32,33], where the curve of M^2 vs. H/M passes through the origin of the plot at the transition temperature. To determine the value of $T_{\rm mag}$, isothermal $M(H)$ curves are measured from 122 to 137 K. The Arrott plot are calculated and shown in Fig. 2(f), which suggests that $T_{\rm mag} \sim 128$ K.

Figures 3(a) and 3(c) show the order parameter plot of the $(1\ 1\ 4)_T$ neutron peak up to 650 K and $(1\ 1\ 0)_T$ neutron peak up to 450 K, respectively and Fig. 3(b) presents the rocking curve scan for the $(1\ 1\ 4)_T$ peak. It is twinned structure below 610 K, so we keep the tetragonal index for convenience. The order parameter plot of the relative stronger peak $(1\ 1\ 4)_T$ [Fig. 3(a)] indicates two phase transitions occurring at 610 and 128 K, respectively. The full data were collected at 4.5, 300, and 650 K to cover all three phase regions. At 650 K, the data can be well fitted in $I41/amd$ symmetry (Table I).

Phosphorus-31 NMR (^{31}P-NMR) measurements were carried out to investigate both transitions. These are summarized in Figs. 3(d)–3(f). In Fig. 3(d), we report the ^{31}P-NMR spectra at various temperatures from 170 to 300 K. ^{31}P nuclear spin $I = 1/2$, and all sites are equivalent for $B \perp ab$. At 300 K, the spectra shift from the Larmor frequency by $K_s = 0.493 \pm 0.002\%$, where the mean and uncertainty were calculated using the gaussian fitting. This value is on the same order of another VPO sample with V^{3+} and about twice as much as that with V^{4+} [34,35], where a similar shift and broadening were observed. The observations are interpreted as evidence for no long range magnetic ordering in the intermediate, charge-ordered phase. Below 190 K, a minor absorption peak

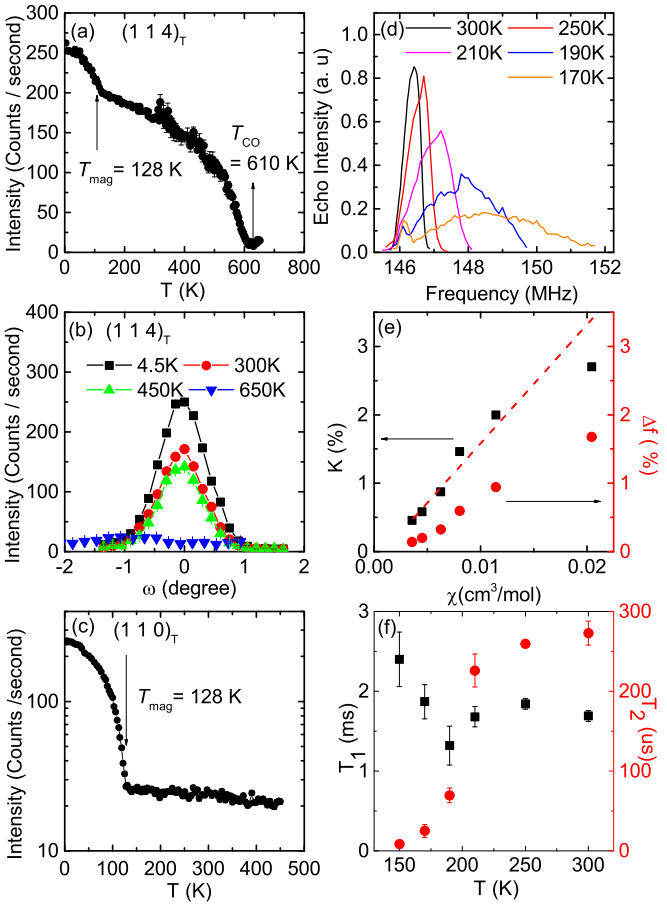

FIG. 3. (a) The $(1\ 1\ 4)_T$ neutron peak intensity vs T. $T_{\rm mag} = 128\,{\rm K}$ and $T_{\rm CO} = 610\,{\rm K}$. (b) The $(1\ 1\ 4)_T$ neutron peak intensity vs ω. (c) The $(1\ 1\ 0)_T$ neutron peak intensity vs T. (d) P NMR frequency spectra. The spectra are conserved after corrections for T_2. (e) Knight shift K and the peak width ΔF obtained from (a) vs magnetic susceptibility χ. Dashed line shows a linear fittings of K. (f) Spin-lattice relaxation time T_1 and spin-spin relaxation time T_2 vs T.

at 146.4 MHz is resolved. Since it accounts for only 3% of the total spin intensities, we expect the signal to be extrinsic due to the sites at twin boundaries and exclude it in our analysis. From the slope of K-χ plot shown in Fig. 3(e), we estimate the hyperfine coupling constant to be $A_{cc} = (10.23 \pm 0.87)$ kOe/μ_B, which is transferred from the unpaired electrons from the second nearest neighbors of P [36]. Figure 3(f) shows the temperature dependence of the spin-lattice relaxation time T_1 and spin-spin relaxation time T_2. The relatively short and constant T_1 is consistent with a paramagnetic phase from 150 to 300 K [37]. Meanwhile, T_2 starts dropping rapidly below 210 K as the system approaches the 128 K transition. This behavior is associated with slow longitudinal fluctuations, which are likely related with the onset of the 128 K magnetic phase transition. This is also consistent with the broadening observed in Fig. 3(d) which appears as the magnetic correlation develops upon cooling. However, since $1/T_2$ is on the order of a few to hundreds of KHz, we conclude that most of our broadening, which is on the order of several MHz, is from the inhomogeneous internal field.

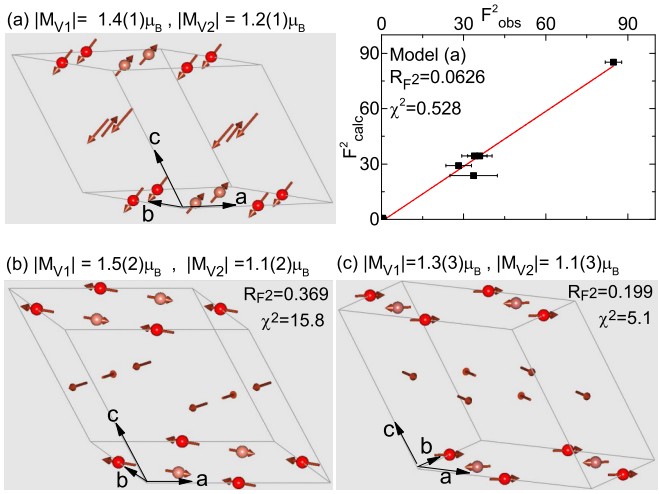

FIG. 4. [(a)–(c)] Three magnetic structure models showing ferrimagnetism with different easy axis. Model (a) is collinear suggesting weak magnetic anisotropy while Models (b) and (c) are noncollinear indicating strong magnetic anisotropy. Model (a) is the magnetic structure of β-V_2PO_5.

The magnetic order onsets at 128 K while the charge order continues to develop below the magnetic transition. Since no observed sharp change can be determined by the structure refinement at 4 K (see Table I), no further structural phase transition below 128 K is discernible. The magnetic propagation vector is $k = 0$, which means that the magnetic scattering signal appears on top of the nuclear Bragg peaks. To determine the magnetic structure more precisely, the magnetic signals were extracted by subtracting the data measured just above 128 K from that at 4 K. During the procedure, to select peaks which are insensitive to the thermal displacements and charge ordering, we compared the data measured at 300 and 450 K and only selected a peak if the change of its intensity is much smaller than the extracted magnetic intensity. The selected reflections are listed in Table II. Since $(1\ 1\ 0)_T$, $(1\ 1\ 4)_T$, $(1\ 0\ 1)_T$, $(0\ 0\ 2)_T$, and $(0\ 0\ 4)_T$ peaks were measured with a long counting time and also tracked upon warming, they are highly reliable as indicated by their small error bars shown in the Table II. We then performed the representational analysis that determines the symmetry-allowed magnetic structures for a second-order magnetic transition. It yielded two magnetic symmetries, $C2/c$ and $C2'/c'$ [23]. Only the $C2'/c'$ can fit our data (see Table II). The obtained magnetic structure is ferrimagnetic. Spins on all V^{2+} (V1 sites) atoms are parallel and so do the spins on all V^{3+} (V2 sites) atoms while these two spin sublattices are antiparallel to each other. Since it is unlikely for the V^{2+} (d^3) to be in a low spin state due to the longer V-O bond length on V1 site and thus weaker crystal electric field, the moment $M_{V1} > M_{V2}$. Figure 4 shows the ferrimagnetic structure with three possible easy axis assignments where $M_{V1} > M_{V2}$. We also did the refinement with the reported model in Ref. [19] by fixing the moment perpendicular to the ab plane. The calculated peak intensity and goodness of fit are summarized in Table II. The model in the left panel of Fig. 4(a) is our pick for the β-V_2PO_5 which gives the best fit of the data as shown in the right panel

TABLE II. Magnetic intensities extracted from neutron scattering refinement for the four models.

h_T	k_T	l_T	F_{2obs}/error	h_M	k_M	l_M	N_{dom}	Fig. 4(a) F_{2cal}(I)	Fig. 4(b) F_{2cal}(II)	Fig. 4(c) F_{2cal}(III)	model in Ref. [19] F_{2cal}(IV)
				2	0	−1	4	0.0408	21.0510	19.1034	0.0000
				0	2	0	3	42.1533	21.0515	19.1039	42.7654
				−2	0	1	2	0.0408	21.0510	19.1034	0.0000
				0	−2	0	1	42.1533	21.0515	19.1039	42.7654
1	1	0	84.75/3.03				1–4	84.3882	84.2051	76.4145	85.5308
				1	−1	0	4	6.9327	2.1990	11.5964	12.3813
				1	1	0	3	10.7699	2.1991	11.5964	9.6339
				−1	1	1	2	10.7699	2.1991	11.5964	9.6339
				−1	−1	1	1	6.9327	2.1990	11.5964	12.3813
1	0	1	33.95/4.62				1–4	35.4051	8.7963	46.3857	44.0304
				1	1	0	4	6.9327	2.1990	11.5964	12.3813
				−1	1	1	3	10.7699	2.1991	11.5964	9.6339
				−1	−1	1	2	10.7699	2.1991	11.5964	9.6339
				1	−1	0	1	6.9327	2.1990	11.5964	12.3813
0	1	1	35.92/4.48				1–4	35.4051	8.7963	46.3857	44.0304
				2	0	1	4	0.0205	10.6680	9.7169	0.0000
				0	2	2	3	15.2162	10.6682	9.7172	8.6145
				−2	0	3	2	0.0205	10.6680	9.7169	0.0000
				0	−2	2	1	15.2162	10.6682	9.7172	8.6145
1	1	4	28.19/4.68				1–4	30.4735	42.6724	38.8682	17.2290
				1	−1	1	4	2.3383	5.7235	8.1520	3.0776
				1	1	1	3	2.3383	5.7235	8.1520	3.0776
				−1	1	2	2	9.3885	5.7235	8.1520	3.7151
				−1	−1	2	1	9.3885	5.7235	8.1520	3.7151
1	0	3	33.65/8.64				1–4	23.4536	22.8940	32.6081	13.5853
				0	0	1	4	0.0003	0.4442	0.0809	0.0000
				0	0	1	3	0.0003	0.4442	0.0809	0.0000
				0	0	1	2	0.0003	0.4442	0.0809	0.0000
				0	0	1	1	0.0003	0.4442	0.0809	0.0000
0	0	2	0.45/1.24				1–4	0.0012	1.7767	0.3234	0.0000
				0	0	2	4	0.0463	0.1722	0.0159	0.0000
				0	0	2	3	0.0463	0.1722	0.0159	0.0000
				0	0	2	2	0.0463	0.1722	0.0159	0.0000
				0	0	2	1	0.0463	0.1722	0.0159	0.0000
0	0	4	0.00/1.00				1–4	0.1853	0.6890	0.0637	0.0000
R_F^2								0.0712	0.369	0.199	0.233
w_F^2								0.0449	0.288	0.164	0.142
R_F								0.0738	0.294	0.111	0.166
χ^2								0.481	15.8	5.10	2.73

of Fig. 4(a). The $M_{V1} = 1.4(1)\mu_B$ and $M_{V2} = 1.2(1)\mu_B$. The easy axis is in ac_M plane and 47(9)° away from a_M towards c_M. The magnetic structure is collinear, suggesting weak magnetic anisotropy. This is indeed consistent with the anisotropic M(H) measurements shown in Fig. 2(c). The other two models shown in Figs. 4(b) and 4(c) are with the easy axis along the chain direction [Fig. 4(b)] or perpendicular to the chain direction on the *ab* plane [Fig. 4(c)]. These two magnetic models are noncollinear with strong magnetic anisotropy. Since the goodness of fit for these two latter models are poor, they are not the right magnetic structure for β-V_2PO_5.

IV. DISCUSSION

It is of particular interest to ask if the charge order is solely responsible for the reduction in the crystal symmetry, or rather if it is a secondary order parameter to some other electronic phase transition. In order to preclude this possibility and elucidate the nature of the charge ordering transition at 610 K, we performed a group theoretical analysis of the lattice distortion using the ISOTROPY SOFTWARE SUITE [38]. The distortion from the high temperature tetragonal structure ($I4_1/amd$) to the low temperature monoclinic structure ($C2/c$) can be caused by two normal modes of lattice vibration, Γ_5^+ and Γ_4^+. Γ_5^+ reduces the symmetry from $I4_1/amd$ to $C2/c$, and is the only

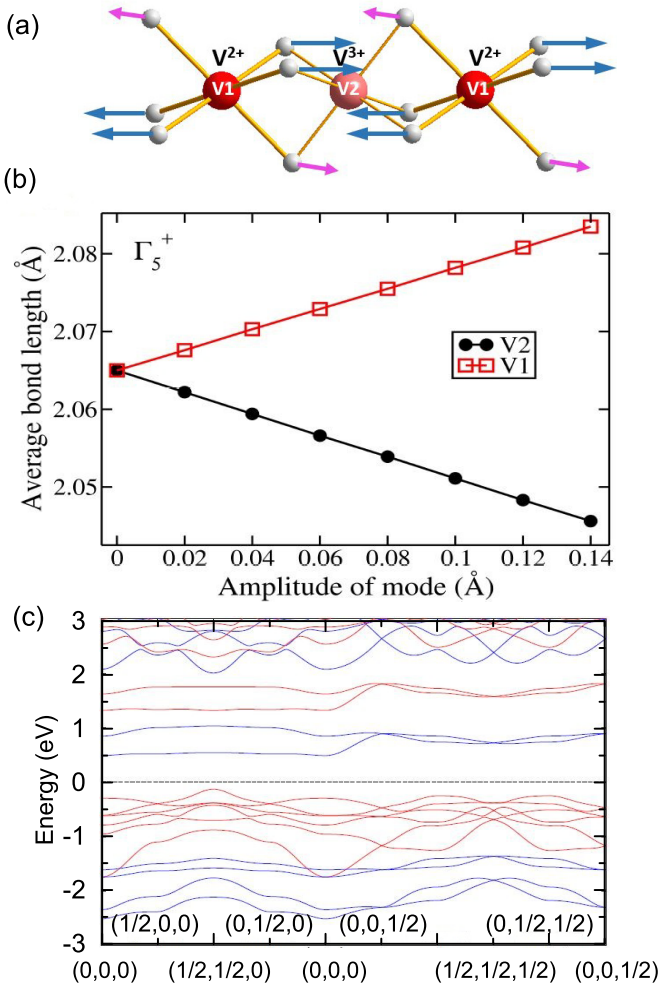

FIG. 5. (a) A sketch of the Oxygen anion displacements due to the Γ_5^+ mode which is responsible for charge ordering. (b) The average V-O bond length as a function of the Γ_5^+ normal mode amplitude. (c) DFT band structure in the ferrimagnetic state. Majority and minority spin bands are shown in red and blue respectively.

candidate for the primary structural order parameter, whereas Γ_4^+ by itself reduces the symmetry to $Fddd$. $C2/c$ is a subgroup of $Fddd$, and as a result, Γ_4^+ is most likely a secondary order parameter that is not important in the energetics of the phase transition. At the same time, the charge order itself, which is a differentiation of the neighboring V ions in the same chain, transforms as the Γ_5^+ irreducible representation does for the high-symmetry structure. Figure 5(a) shows the displacement of the oxygen atoms in the VO_6 face-sharing chain due to the Γ_5^+ normal mode. This mode breaks the symmetry between the V ions that are symmetry equivalent at $I4_1/amd$, and decreases the V-O bond length for V_2 while increasing it for V_1 [Fig. 5(b)] as expected in a charge ordering transition. We therefore conclude that to reduce the symmetry to the monoclinic phase, the charge order, by itself, is sufficient and no other magnetic or electronic mechanisms are necessary. This is consistent with the fact that the T_{CO} is almost 5 times of the T_{mag}. We also note that Γ_5^+ is a Raman active mode, and as a result, signature of the charge ordering transition should be visible in the Raman spectrum of β-V_2PO_5.

TABLE III. Energies of different magnetic configurations from first principles.

Intrachain	Interchain	Energy (meV/f.u.)
Ferrimagnetic	Ferromagnetic	0
Ferrimagnetic	Antiferromagnetic	9
Ferromagnetic	Ferromagnetic	60
Ferromagnetic	Antiferromagnetic	71

We performed the first-principles calculation using DFT + U with $U = 4$ eV to correct for the underestimation of the on-site coulomb interaction on the V ion [39]. Our DFT calculations predict magnetic moments of 2.6 μ_B and 1.8 μ_B respectively inside the V_1 and V_2 spheres, but the band structure [Fig. 5(c)] shows no partially filled bands. This signals strong hybridization between the V and the O ions. DFT gives a magnetic moment 0.5 μ_B per V including the interstitials. This is a strong overestimation compared to the experimental value. The reason of this is likely the DFT + U's tendency to overestimate the ordered moments when there are dynamical fluctuations present, and it is possible that a more advanced first-principles method (such as the dynamical mean-field theory) can reproduce the experimentally observed value of the local moments.

To understand the magnetic order, we calculated the energies of phases with different magnetic orders from DFT, as listed in Table III. The lowest energy phase is predicted to have ferrimagnetic intrachain order, where the moments of the neighboring V_1 and V_2 ions on the same chain are aligned antiparallel, and ferromagnetic interchain order, so that, for example, the magnetic moments of all V_1 ions are parallel. This calculated result is in line with the experimental observation. The energy cost of having a magnetic phase where the different chains have antiparallel moments is about 9–10 meV per formula unit, whereas the energy cost of having spins on the same chain parallel is 60 meV per formula unit. This suggests that the intrachain interactions between the V_1 and V_2 ions in the face-sharing VO_6 chains are the dominant term in the magnetic Hamiltonian.

To understand the crossover behavior in H/M shown in in Fig. 2(b), we calculated the energetics of different magnetic phases in the high temperature tetragonal structure ($I4_1/amd$) with the same parameters (not shown), and found that similar couplings apply to magnetic moments in that structure too. This explains the crossover: above the charge ordering temperature, the magnetic moments on all V ions are equal, and its Curie-Weiss behavior is that of an antiferromagnet, with a negative Curie temperature. However, charge ordering makes the moments unequal, and as a result, below 610 K the Curie-Weiss behavior is that of an ferrimagnet, which has a positive Curie temperature like a ferromagnet.

To address if there is nontrivial topology in this compound, the DFT band structure in Fig. 5(c) is calculated in the ferrimagnetic ground state. Unlike the DFT band structure calculated in the ferromagnetic phase and the tetragonal structure without U [17], there are no band crossing at the Fermi level. And more importantly, the top of the valence and the bottom

of the conduction bands have opposite spin directions. This observation precludes any possibility of topological phases in β-V_2PO_5.

V. CONCLUSION

In conclusion, the charge ordering and ferrimagnetism in the β-V_2PO_5 single crystals are confirmed by transport, magnetic, specific heat, single crystal neutron diffraction and NMR measurements. Below 610 K, the single V site at the high temperature tetragonal phase distorts into two alternating V sites, leading to the increase of V-O bond length of one V site but the decrease of the other V site. Our first-principles calculation shows that this distortion was caused by the Γ_5^+ normal mode of lattice vibration. Accompanied with the distortion, charge ordering of V^{2+} and V^{3+} is undoubtedly suggested by the Bond-valence analysis. Below 128 K, the spins order parallel on each sublattice of V sites while the spins on one sublattice order antiparallel to the other. With the easy axis being in the monoclinic *ac* plane and 47(9)° away from the monoclinic *a* towards *c* axis, this gives a collinear ferrimagnetic structure with the moment to be $1.4(1)\mu_B$ on V^{2+} site and $1.2(1)\mu_B$ on V^{3+} site, suggesting weak magnetic anisotropy and dominant role of the intrachain V-V interaction in magnetism. No nontrivial topology is suggested by our first-principles calculations, and the experimentally observed insulating phase goes against the possibility of a Weyl semimetal phase.

ACKNOWLEDGMENTS

Work at UCLA (J.X., C.W.H., R.C., N.N.) was supported by NSF DMREF program under the award NSF DMREF project DMREF-1629457. Work at ORNL HFIR was sponsored by the Scientific User Facilities Division, Office of Science, Basic Energy Sciences, U.S. Department of Energy. Work at UMN was supported by NSF DMREF program under the award NSF DMREF project DMREF-1629260. Work at UCLA (H.H.W., Y.K.L., S.B.) was supported by NSF DMR-1410343 and DMR-1709304. Y.K.L. would also like to thank the support from LANL LDRD program.

[1] J. Attfield, Solid State Sci. **8**, 861 (2006).
[2] E. Wollan and W. Koehler, Phys. Rev. **100**, 545 (1955).
[3] J. Goodenough, Phys. Rev. **100**, 564 (1955).
[4] T. Yamauchi, M. Isobe, and Y. Ueda, Solid State Sci. **7**, 874 (2005).
[5] R. Glaum, M. Reehuis, N. Stüßer, U. Kaiser, and F. Reinauer, J. Solid State Chem. **126**, 15 (1996).
[6] J. Kikuchi, N. Kurata, K. Motoya, T. Yamauchi, and Y. Ueda, J. Phys. Soc. Jpn. **70**, 2765 (2001).
[7] J. Johnson, D. Johnston, H. King Jr., T. Halbert, J. Brody, and D. Goshorn, Inorg. Chem. **27**, 1646 (1988).
[8] D. C. Johnston, J. W. Johnson, D. P. Goshorn, and A. J. Jacobson, Phys. Rev. B **35**, 219 (1987).
[9] E. Dagotto, J. Riera, and D. Scalapino, Phys. Rev. B **45**, 5744 (1992).
[10] A. W. Garrett, S. E. Nagler, D. A. Tennant, B. C. Sales, and T. Barnes, Phys. Rev. Lett. **79**, 745 (1997).
[11] J. Kikuchi, K. Motoya, T. Yamauchi, and Y. Ueda, Phys. Rev. B **60**, 6731 (1999).
[12] T. Yamauchi, Y. Narumi, J. Kikuchi, Y. Ueda, K. Tatani, T. C. Kobayashi, K. Kindo, and K. Motoya, Phys. Rev. Lett. **83**, 3729 (1999).
[13] E. Kaul, H. Rosner, N. Shannon, R. Shpanchenko, and C. Geibel, J. Mag. Mag. Mater. **272**, 922 (2004).
[14] R. Nath, A. A. Tsirlin, H. Rosner, and C. Geibel, Phys. Rev. B **78**, 064422 (2008).
[15] A. A. Tsirlin, R. Nath, A. M. Abakumov, R. V. Shpanchenko, C. Geibel, and H. Rosner, Phys. Rev. B **81**, 174424 (2010)
[16] R. Glaum and R. Gruehn, Z. Kristallogr. **186**, 91 (1989).
[17] Y. J. Jin, R. Wang, Z. J. Chen, J. Z. Zhao, Y. J. Zhao, and H. Xu, Phys. Rev. B **96**, 201102(R) (2017).
[18] E. Elkaïm, J. F. Berar, C. Gleitzer, B. Malaman, M. Ijjaali, and C. Lecomte, Acta Cryst. **B52**, 428 (1996).
[19] E. Pachoud, J. Cumby, C. T. Lithgow, and J. Attfield, J. Am. Chem. Sov. **140**, 636 (2018).
[20] K. Murota, E. Pachoud, J. Attfield, R. Glaum, R. Sutarto, K. Takubo, D. Khomskii, and T. Mizokawa, Phys. Rev. B **101**, 245106 (2020).
[21] D. Smith and F. Fickett, J. Res. Natl. Inst. Stand. Technol. **100**, 119 (1995).
[22] B. Chakoumakos, H. Cao, F. Ye, A. Stoica, M. Popovici, M. Sundaram, W. Zhou, J. Hicks, G. Lynn, and R. Riedel, J. Appl. Crystallogr. **44**, 655 (2011).
[23] A. Wills, Phys. B: Condens. Matt. **276**, 680 (2000), program available from www.ccp14.ac.uk.
[24] J. Rodriguez-Carvajal, Phys. B: Condens. Matt. **192**, 55 (1993).
[25] E. Fukushima and S. B. Roeder, *Experimental Pulse NMR* (Westview, 1993).
[26] G. Kresse and J. Furthmüller, Phys. Rev. B **54**, 11169 (1996).
[27] G. Kresse and J. Hafner, Phys. Rev. B **48**, 13115 (1993).
[28] J. P. Perdew, A. Ruzsinszky, G. I. Csonka, O. A. Vydrov, G. E. Scuseria, L. A. Constantin, X. Zhou, and K. Burke, Phys. Rev. Lett. **100**, 136406 (2008).
[29] N. Brese and M. O'keeffe, Acta Crystallogr. Sect. B: Struct. Sci. **47**, 192 (1991).
[30] I. David Brown, Bond valence parameters, https://www.iucr.org/resources/data/datasets/bond-valence-parameters.
[31] M. Khan, R. Harani, M. Ahmed, and C. Hogarth, J. Mater. Sci. **20**, 2207 (1985).
[32] A. Arrott, and J. Noakes, Phys. Rev. Lett. **19**, 786 (1967).
[33] M. Halder, S. M. Yusuf, M. D. Mukadam, and K. Shashikala, Phys. Rev. B **81**, 174402 (2010)
[34] M. Sananes and A. Tuel, Solid State Nucl. Magn. Reson. **6**, 157 (1996).
[35] M. Sananes, A. Tuel, and J. C. Volta, J. Catalys. **145**, 251 (1994).
[36] J. Li, M. Lashier, G. Schrader, and B. Gerstein, Appl. Catalys. **73**, 83 (1991).
[37] T. Moriya, Prog. Theor. Phys. **16**, 23 (1956).
[38] H. Stokes, D. Hatch, and B. Campbell. Isotropy. Retrieved from stokes.byu.edu/isotropy.html (2007).
[39] A. I. Liechtenstein, V. I. Anisimov, and J. Zaanen, Phys. Rev. B **52**, R5467 (1995).